Final Report

1. DOE Award Number

DE-SC0005713, (SUNY RF number 56846)

2. Project Title and Name of PI

Photocathodes for High Repetition Rate Light Sources

PI Ilan Ben-Zvi
Department of Physics and Astronomy
and the Center for Accelerator Science and Education
Stony Brook University

3. Date of Report and Period Covered by the Report

Final report, dated April 20, 2014 for the period January 1, 2011 through December 31, 2013

4. Discussion of Accomplishments

4.1 The collaboration

This proposal brought together teams at Brookhaven National Laboratory (BNL), Lawrence Berkeley National Laboratory (LBNL) and Stony Brook University (SBU) to study photocathodes for high repetition rate light sources such as Free Electron Lasers (FEL) and Energy Recovery Linacs (ERL). Below details the Principal Investigators and contact information. Each PI submits separately for a budget through his corresponding institute.

Principal Investigators

Ilan Ben-Zvi: Faculty, Stony Brook University, Physics Building, Stony Brook, NY 11794-3800
Phone (631) 632 8100: Ilan.Ben-Zvi@stonybrook.edu
John Smedley: Staff Scientist: Brookhaven National Laboratory, MS-535B, Upton, NY 11973-5000:
Phone (631) 344 7865: Fax (631) 344 5773: smedley@bnl.gov Point of contact and coordinator for the
combined research activity.
Howard Padmore: Senior Staff Scientist: Lawrence Berkeley National Lab, MS 2-400, Berkeley CA 94720:
Phone (510) 486 5787: Fax (510) 485 7696: HAPadmore@lbl.gov

The work done under this grant comprises a comprehensive program on critical aspects of the production of the electron beams needed for future user facilities. Our program pioneered *in situ* and *in operando* diagnostics for alkali antimonide growth. The focus is on development of photocathodes for high repetition rate Free Electron Lasers (FELs) and Energy Recovery Linacs (ERLs), including testing SRF photoguns, both normal-conducting and superconducting. Teams from BNL, LBNL and Stony Brook University (SBU) led this research, and coordinated their work over a range

of topics. The work leveraged a robust infrastructure of existing facilities and the support was used for carrying out the research at these facilities. The program concentrated in three areas:

a) Physics and chemistry of alkali-antimonide cathodes (BNL – LBNL)
b) Development and testing of a diamond amplifier for photocathodes (SBU - BNL)
c) Tests of both cathodes in superconducting RF photoguns (SBU) and copper RF photoguns (LBNL)

Our work made extensive use of synchrotron radiation materials science techniques, such as powder- and single-crystal diffraction, x-ray fluorescence, EXAFS and variable energy XPS. BNL and LBNL have many complementary facilities at the two light sources associated with these laboratories (NSLS and ALS, respectively); use of these will be a major thrust of our program and bring our understanding of these complex materials to a new level. In addition, CHESS at Cornell will be used to continue seamlessly throughout the NSLS dark period and new diffraction facilities at ALS will be utilized. We also will continue to make use of the excellent analytical facilities at the CNF (BNL) and the Molecular Foundry (LBNL), where we have access to state of the art UHV XPS, SPM, SEM and scanning Auger microscopy.

This R&D program leveraged enormous assets at the three institutions. At the synchrotron radiation facilities, we have most of the analytical tools we used. We have developed systems for *in situ* and *in operando* x-ray analysis, as well as for transportation of samples between deposition chambers and the various tools.

4.2 Accomplishments

In this section we outline the rationale for the work carried out under this proposal, and review progress we've made during the grant's three years.

4.2a) Cathode Background

The selection of the cathode material and the corresponding laser is dictated by the beam current and emittance requirements of the application. The operating range of the cathode and the corresponding drive laser system can be divided in to three distinct regimes: < 1 μA, 1 μA – 1 mA, and > 1 mA. Metal photocathodes have proven to be highly suitable for low repetition rate, high peak brightness injectors with current < 1 μA[3]. With sufficient laser research this limit can be pushed to the 10 μA regime. However, as the repetition rate/bunch charge is increased further, the low QE and large photon energy requirements inherent to these cathodes put an inordinate stress on the laser development, well beyond the current state-of-the-art. The focus then shifts to cathode materials with high QE at longer wavelengths, preferably in the visible, due to the need to use efficient longitudinal and transverse beam shaping techniques. In the past decade, there has been considerable research in NEA and PEA semiconductor cathodes such as GaAs:Cs, GaN:Cs, CsTe and multi-alkali cathodes. The research interest has shifted to the development of reliable, long-lived photocathodes with fast time response and high levels of reproducibility.

GaAs:Cs has been used with DC guns at JLab to deliver over 900 hours and 7000 Coulombs at 2-9 mA CW from a single GaAs wafer between 2004 and 2007 with a lifetime of 550 Coulombs or 30 hours at an average current of 5 mA CW [4]. The major limitations of this cathode are the reduction in lifetime due to ion back bombardment in the DC environment and the long response time for 530 nm radiation. In order to reduce the ion bombardment, the operating vacuum for these cathodes needs to be in the low 10^{-11} Torr range. Since the photon absorption length and escape depth of the electrons are long for 2.3 eV photons, the electron bunch length does not match the pulse duration of the photon, but has a decay commensurate with the electron transport from deeper layers of the cathode. These cathodes have been tested primarily in DC guns, and their performance in an RF injector has not yet been tested.

Cs_2Te has been used in normal conducting guns at FLASH, PITZ and in an SRF gun at Rossendorf. At PITZ, this cathode has delivered ~ 1 mA in a macropulse of 700 μs duration [5]. At Flash, these cathodes routinely deliver 3-4% QE (higher pre-transport at INFN) at 254 nm. This material is therefore undoubtedly a good candidate material, but is not proven at high rep rate and average current. In addition, it requires frequency quadrupling from YAG wavelengths compared to the doubling required for alkali antimonides and GaAs:Cs, requiring higher average laser power. In addition, precise transverse and temporal shaping in the UV is significantly more difficult than in the visible region.

A K_2CsSb cathode has been used in an RF injector of an FEL for the first time at Boeing- Los Alamos, delivering 47 mA in a macropulse of 10 ms duration with a duty factor of 25% [6].The lifetime of the cathode in this measurement was dependent on the partial pressure of water vapor in the vacuum and was extrapolated to be longer than 10^4 hours for a partial pressure of 10^{-12} Torr. This cathode material has also been used in streak cameras to measure the pulse duration of ultra-short optical pulses, indicating the prompt response of the material. The original Boeing-Los Alamos work was hindered by poor vacuum in the high frequency RF gun, and specifically high partial pressures of water. This limited the cathode lifetime to only 10 hrs in the gun itself, but together with measurements of lifetime v. water pressure in the preparation chamber, did indicate that if good UHV conditions could be achieved, this material would satisfy most of the requirements for a high repetition rate, high current injector. With the advent of superconducting cavities with naturally excellent vacuum characteristics and very well pumped VHF guns with more open geometry, this opens the way to the use of this material, however, we need to measure and understand many of its materials characteristics to validate that indeed it will work in practice.

In a diamond amplifier (DA), electrons from a primary source are accelerated to a few keV to impinge on the metalized face of a high purity, single crystal diamond. The primary electrons lose their energy via inelastic collision to create multiple e-h pairs. An external field is applied to the diamond at the appropriate time to sweep

the secondary electrons towards the opposite face of the diamond. This face is hydrogenated to reduce the electron affinity such that, upon arriving at this surface, the secondary electrons are readily emitted into the accelerating field. The large band gap of the diamond and the high mobility of both the electrons and holes provide a large mean free path to the electrons in the conduction band, increase the breakdown field, and minimize the dark current from the cathode as well as e-h recombination. The high saturation velocities of the carriers reduce the broadening of the electron bunch length. The high thermal conductance of diamond enables the removal of heat generated by both the RF field in a RF injector and the electron beam. The diamond itself also forms an effective barrier between the sensitive cathode and the RF cavity minimizing the contamination of both. More importantly, the diamond amplifier's performance is independent of the primary electron source, hence it would be usable with any cathode to increase the beam current.

The performance of the DA depends critically on a number of parameters, including the characteristics of the metal-diamond interface, the bulk diamond, and the hydrogen termination, as well as their impact on secondary electron generation, transport and emission. Each of these has to be addressed and optimized. In addition, engineering aspects of combining the DA with the primary electron source and integration of the DA into a RF injector also need to be addressed before the DA can be tested in an injector.

4.2b) Overview of our work on diamond amplifiers and alkali antimonides

4.2bi) Diamond Amplifiers

One method to reach the average currents required by future light sources may be to use a standard photocathode, such as K_2CsSb, in conjunction with an "amplifier" to increase the emitted current while retaining the small phase space volume of the photocathode. One such device, based on diamond, has been proposed [7]; this device uses low energy (few keV) electrons (potentially accelerated from a photocathode source) to produce carriers in diamond. The diamond is biased such that electrons drift toward the emitting surface, which has a negative electron affinity due to hydrogen termination [8] . The electrons are emitted through the NEA surface into the accelerating cavity. As an initial primary electron can produce hundreds of secondary electrons, this device has the potential to greatly increase the available current for a linac-based source.

The development of diamond as an electron amplifier has proceeded along three avenues of inquiry: first, the study of the material properties of the diamonds used, including impurity content and crystalline defects [9], second, the characterization of charge transport in bulk diamond with electrodes on both sides, and third, the characterization of the emission of electrons from the NEA surface. This work has been supported by a modeling effort [10] which has used Monte Carlo techniques along with the full band structure of diamond to simulate the production and propagation of carriers.

Charge transport has been investigated using both electron- and x-ray-generated carriers. For x-ray-generated carriers, this resulted in the fabrication of prototype diamond x-ray detectors [11-13]. These devices are typically made from ultra-high purity single crystal CVD diamond, 4x4 mm^2 with a thickness between 0.3 and 0.5 mm. The surface normal is [100], and the large surfaces are polished to ~2 nm rms surface roughness. Using 5 beamlines at the NSLS, the response of the diamond to x-ray photons from 0.2-28 keV has been measured, with incident flux ranging from 100 pW to 10 W, and is in good agreement with theoretical predictions. Understanding the diffusion of carriers created with photons near the carbon edge is critical for understanding the performance of diamond using electron generated carriers, as these carriers will be produced in a region ~100 nm from the incident electrode, comparable to those produced by 400 eV photons.

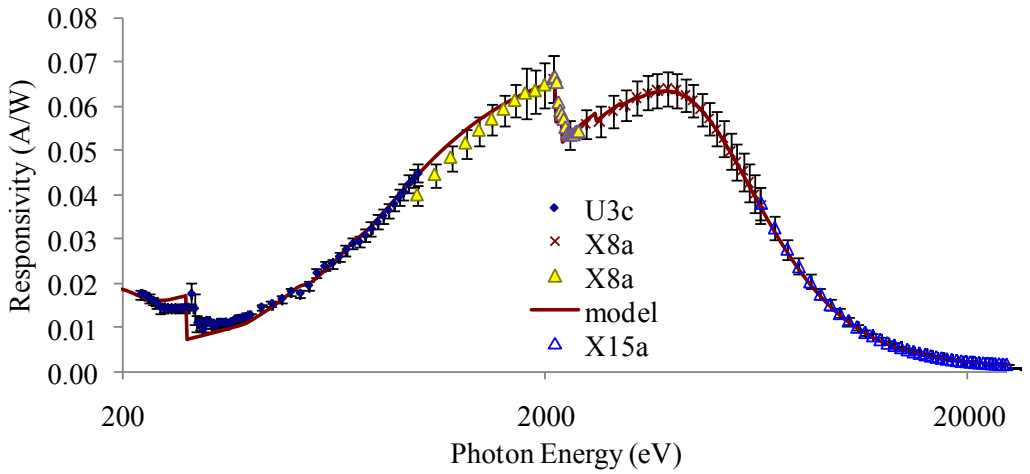

Fig. 1 Responsivity vs. photon energy for a 260 μm thick oxygen-terminated diamond with 40 nm thick platinum contacts. 200 V bias on incident electrode was used (hole bias), with 1 kHz, 95% duty cycle for energies up to 1 keV and 100% duty cycle beyond 1 keV.

To test the current density required for the electron amplifier, a focused "white" x-ray beam was used to generate an average current of 85 mA in an area of 1.1x0.6 mm^2; this corresponds to an average current density of 13 A/cm^2 – roughly an order of magnitude higher than is envisioned for a diamond amplified cathode operating at a storage-ring equivalent current (~0.5 A).

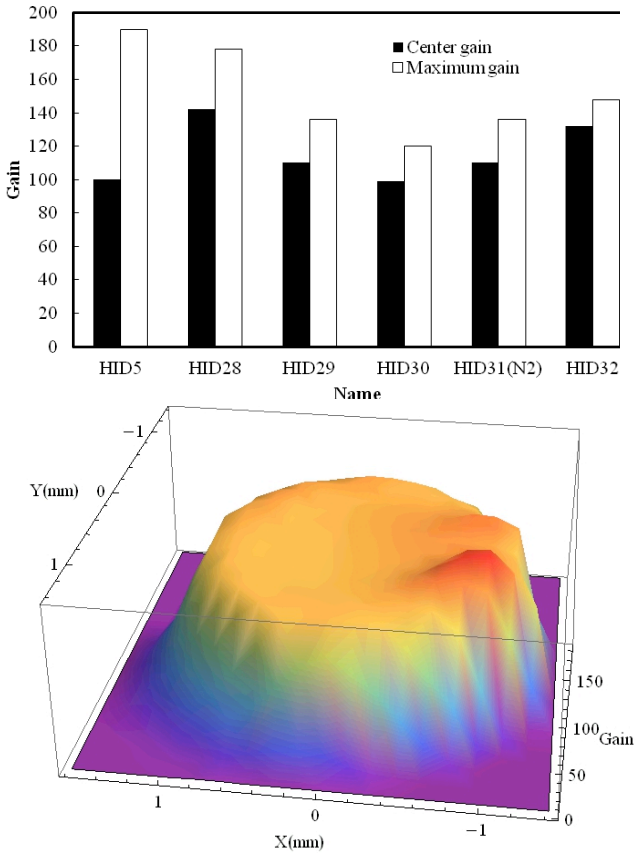

Fig. 2 Left: The gain in six different diamond amplifiers. The black columns show the gain of the centers of the diamond amplifiers, and the white columns show the maximum gain on the samples. Right: Gain uniformity of an amplifier.

Electron emission from diamond has been observed using both photon- and electron-generated carriers [14, 15]. For electron-generated carriers, emitted electrons have been imaged on a phosphor screen (fig. below). A maximum gain of 140 has been reproducibly observed, roughly 65% of the expected value based on transmission measurements (figures above). Some insight into this loss is obtained by comparing the results with emission from X-ray-generated carriers. Here the emitted current was less than 1% of the expected value (fig. below). The principle difference between these systems is the vacuum level (sub nTorr for the electron beam system, ~100 nTorr for the X-ray system), suggesting that the negative electron affinity surface of the diamond is susceptible to contamination. This observation is consistent with angle resolved photoemission spectroscopy (ARPES) measurements on diamond (fig. below), which clearly demonstrate a NEA peak after a 400 C bake; this peak disappears on a timescale of a few hours in a 0.1 nTorr vacuum (and can be subsequently recovered with another 400 C bake). It is unknown whether the initial hydrogenation procedure used on the diamond affects this lifetime or what gasses in the vacuum system are most critical, although water is suspected. The

long-term stability of the surface seems to be very good, however. A diamond has been stored in air for more than a year, and recovered emission with only an in-vacuum bake.

The diamond ARPES measurements [16] have provided insight into the emission process from NEA diamond. As diamond is an indirect band material, not all of the momentum states which form the conduction band minimum allow an electron to achieve sufficient perpendicular momentum to escape the surface. These electrons would be effectively trapped at the diamond surface, except that a phonon-assisted emission process exists which leads to emission of electrons with energy bands separated by one optical phonon energy (145 meV).

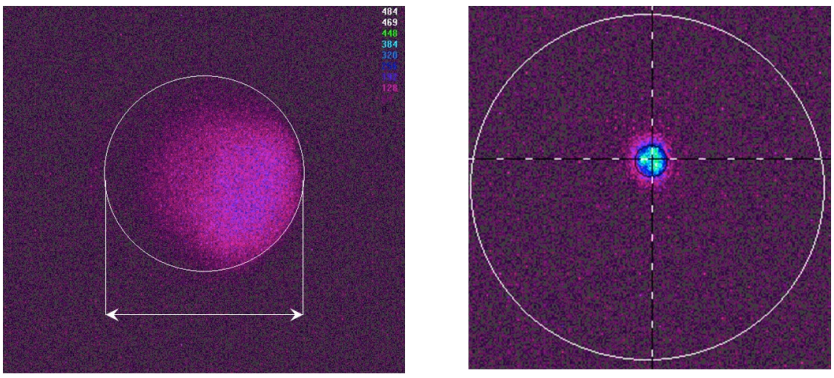

Without focusing

With focusing and reduced primary current

Electron beam emitted from a diamond amplifier

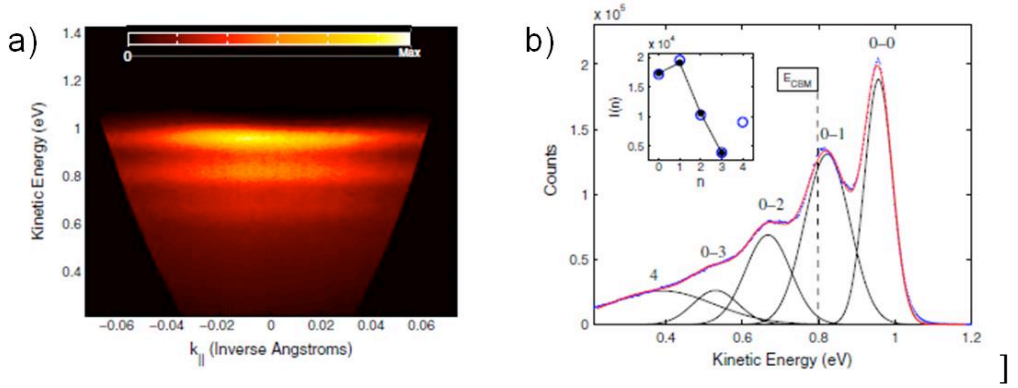

Fig. 3 a) ARPES spectrum acquired using the 6.01eV laser. The color bar shows relative intensity. The overall "bowl" shape of the spectrum results from scaling between emission angle and k‖ b) Energy distribution curve. Blue points show data and the line through the points is the total fit. The decomposition of the fit into constituent Gaussian curves is shown for comparison.

Diamond/Metal interface:

In our previous work it was observed that electron trapping near the diamond surface could lead to photoconductive gain in current mode devices [16]. In a recent *Applied Physics Letters* publication, we identified that the Schottky barrier at the diamond-metal interface can be modified by appropriate selection of metal contact and surface termination to eliminate unwanted charge injection. The Schottky barrier of the back contact in the DA is responsible for charge resupply of both electrons (during the emission phase) and holes (during the de-trapping phase). The Schottky barrier for various contact materials has been determined and it is reported that non carbide-forming metallic contacts such as platinum, along with oxygen termination, provide a blocking contact to hole injection into diamond. While investigating the spatial uniformity of the diamond response to x-rays, it was observed that platinum contacts prepared on oxygen terminated diamond provided a uniform response, however, upon annealing these devices to ~500°C, the uniformity was lost giving rise to hot spots in the response.

Using hard x-ray photoelectron spectroscopy (HAXPES) and the Kraut's method [17] for measuring the band offsets, it was determined that annealing alters the oxygen termination of the diamond and lowers the Schottky barrier allowing the injection of holes (Fig. below (a)). In addition, we measured the Schottky barrier of an unannealed silver-diamond interface and determined that the Schottky barrier is never sufficient to block the injection of holes, which matches our observation that silver contact exhibited hot spots regardless of the diamond surface termination. The position of the diamond valence-band maximum was determined by theoretically calculating the diamond density of states and applying cross section corrections (Fig. (b)). The diamond-platinum Schottky barrier height was lowered by 0.2 eV after thermal annealing, indicating annealing may increase carrier injection in diamond devices leading to photoconductive gain. The platinum contacts on oxygen-terminated diamond was found to provide a higher Schottky barrier and therefore a better blocking contact than that of the silver contact in diamond-based electronic devices. In addition, we have identified that direct photoemission from this back contact, caused by the high energy incident electron (or photon) beam can inject electrons into the diamond and contribute charge to the device. The contribution of this charge in the operation of the DA is currently under investigation.

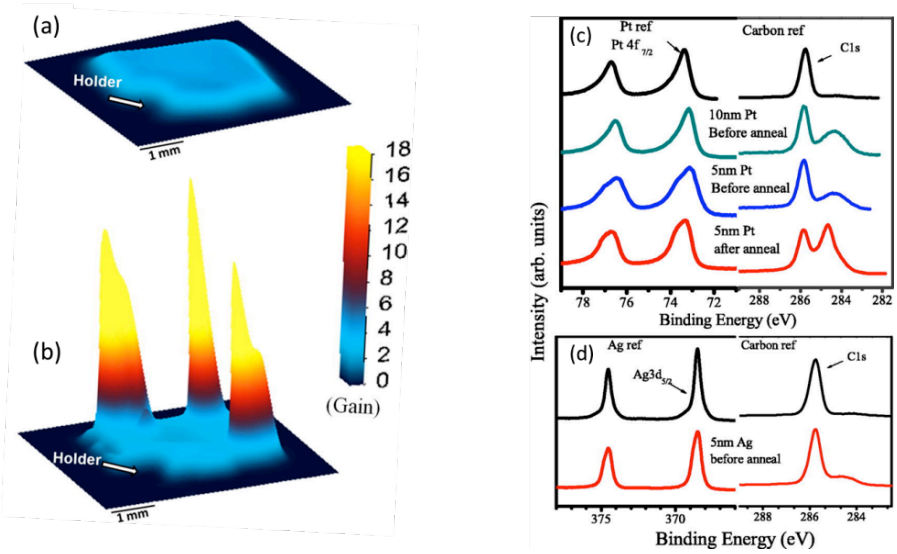

Fig. 4. Diamond response (normalized by upstream monitor signal) (a) before and (b) after anneal. A bias voltage of −100 V was applie for both measurements. (c) HAXPES spectrum of Pt4f, (d) Ag3d (bottom left) and C1s core-levels (right). Arrows indicate the peaks used for band alignment. The core lines are referenced to the Fermi level of Au.

An alternative to metal contacts is to use a thin patterned layer of conductive nitrogen doped ultrananocrystalline diamond (UNCD). The UNCD material was developed by colleagues at the Center for Nanoscale Materials at Argonne National Laboratory and we have successfully incorporated it as a contact material on single crystal diamond. The contact retains most of the important characteristics of diamond, specifically its radiation hardness, thermal conductivity, strength, and low density. A UNCD contact offer several advantages to metal. When used in the DA, the low density would reduce the energy loss of the primary electrons as they pass through the incident contact. The contact also forms a robust ohmic contact providing a low barrier to charge resupply. Finally, the high thermal conductivity can efficiently remove heat from the device as the current in the diamond increases.

Hydrogen Termination Diagnostics and Optimization

A diagnostic based on UV photoemission has been developed to evaluate the performance of the "hydrogenation" procedure without needing to test a full amplifier. This was used to optimize the hydrogenation procedure to increase the lifetime vs. contamination, leading to a high temperature activation process of the diamonds in an atomic hydrogen environment. The decay curve of the room temperature hydrogenation has two components, one with a decay time of 0.25 hours, and a slower component where the decay time is ~4.76 hours. This slow decay component is common to both room temperature and high-temperature process curves (figure below, right). This loss of photocurrent can be recovered by baking the sample. Thus, after the decay of the photocurrent over 11 hours, the diamonds were baked at 400 C for 30 minutes. There was

almost full recovery (99%) of the photocurrent of the diamond that underwent high-temperature hydrogenation; the decay of the photocurrent under this condition is due to contaminants, such as water absorbed on the hydrogenated surface that are desorbed to the surface during baking[18, 19]. However, the photocurrent of the diamond hydrogenated at room temperature exhibited only 65% recovery after baking, implying that baking can correct the slow decay, but not that lost during the fast decay.

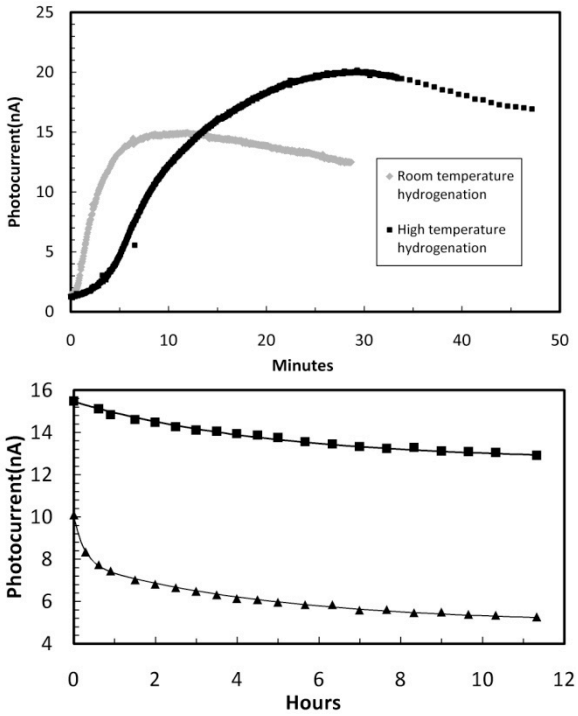

Fig. 5 Left: The trend in the photocurrent during the hydrogenation process. Dark curve: trend during high-temperature hydrogenation; gray curve: room temperature hydrogenation. Right: The stabilization of the photocurrent of hydrogenated diamonds. Solid squares: photocurrent of the high-temperature-treated diamond; solid triangles: photocurrent of hydrogenation decay at room temperature.

LBNL test of Diamond Amplifier in NCRF VHF gun

A first test of a diamond amplifier was performed in the ALS 185 MHz normal conducting RF gun at LBNL. The initial observation indicated that emission from hydrogenated diamond is possible in an RF field. The figure below shows the schematic drawing of the holder. The incident laser beam passes through the metal coated hydrogenated diamond and illuminates the copper cathode. Under an 8KV bias, the primary electrons emitted from the cathode travel through the gap between the cathode and the metalized surface of the diamond and hit the diamond from the back. Secondary electrons generated from such bombardment and drifted under the force exerted by an RF field in the cavity towards the hydrogenated surface of diamond are eventually emitted from the NEA surface into the RF cavity.

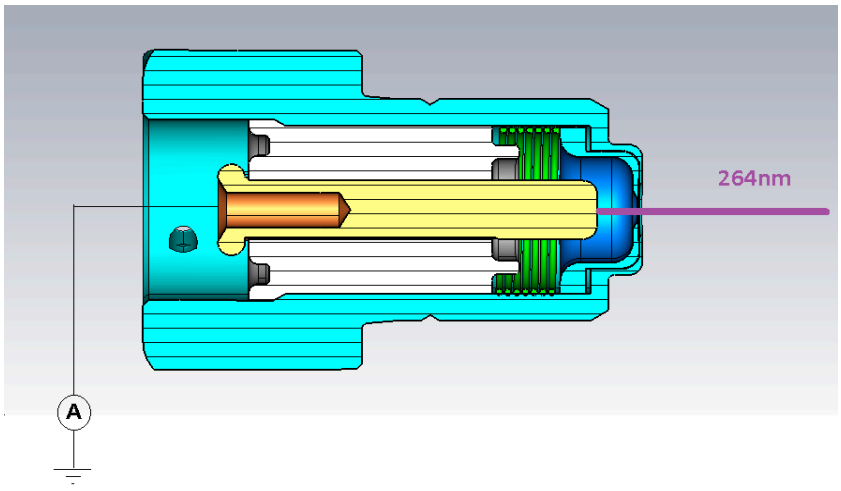

Fig. 6 Diamond holder with primary cathode. Yellow: copper primary cathode, white: alumina insulator, blue: aluminum, green: stainless steel spring that ensures the good electric contact for the sake of RF sealing. The diamond is located at the tip of the holder (far right) and is the first component illuminated by the incident laser beam.

Electron emission from the diamond was observed, however it is uncertain whether this emission resulted from amplification of primary electrons or from emission directly from the diamond. It is likely that one of the two beams observed is the electron photoemission from the hydrogenated surface of diamond (figure below). The occasional second beam (figure below, left) observed at some rf phases may result from electron injection from the Pt layer into diamond and subsequent emission of the injected electrons.

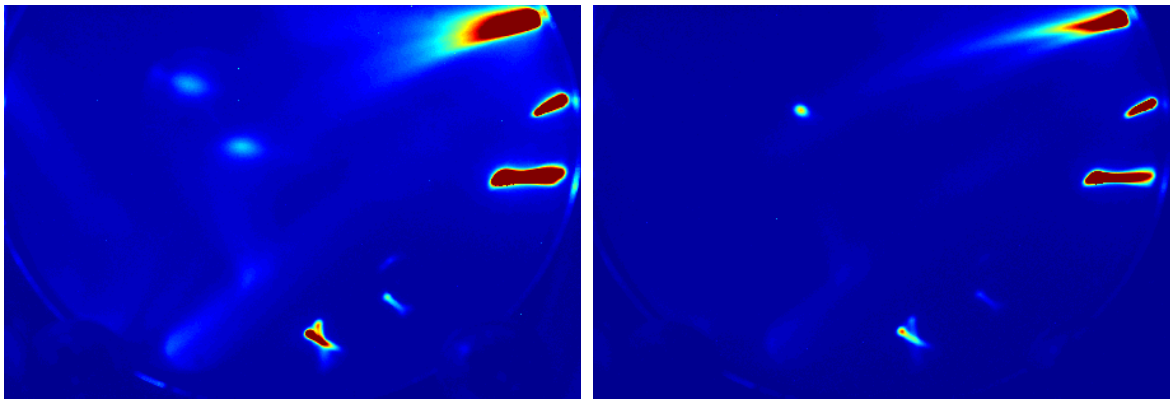

Fig. 7 Beam spot captured on YAG screen 1.5 m away from the diamond. Beam generated from laser illumination is the spot located near upper left corner. The other butterfly shaped spots are dark current. The most noticeable feature is that under certain laser phases, there are two beams on the screen simultaneously.

From this experiment, the team has gained experience with testing the diamond amplifier in the RF gun. This has provided critical insight into RF requirements for the holder design and RF effects on the performance of the diamond amplifier. This has also provided an opportunity to evaluate the effects of high powered 266 nm laser on the diamond surface as well as the effects of RF fields on the Pt coating on the back of the diamond.

4.2bii) Alkali Antimonides

The alkali antimonides are a broad class of materials, some of which have extraordinary photo-emissive properties. They can be split into the mono-, bi- and multi-alkali antimonides, with the latter in general having a response further into the infrared part of the spectrum. Of these, the bi–alkalis containing potassium and cesium appear to be some of the most useful in terms of high quantum yield at low energy. The discovery of the alkali antimonides dates back to the 1930s [20] and beyond, but in the late 1950s, their development accelerated due to the importance of the materials in photomultiplier tubes and in infrared imaging devices. One of the early pioneers of this work was A. H. Sommer, and his book 'Photoemissive Materials' contains a comprehensive review of alkali antimonide research up to the late 1960s [21]. Here we will concentrate on the properties of the bi-alkali antimonides as they have the most appropriate response for photoinjector applications, and review their basic properties.

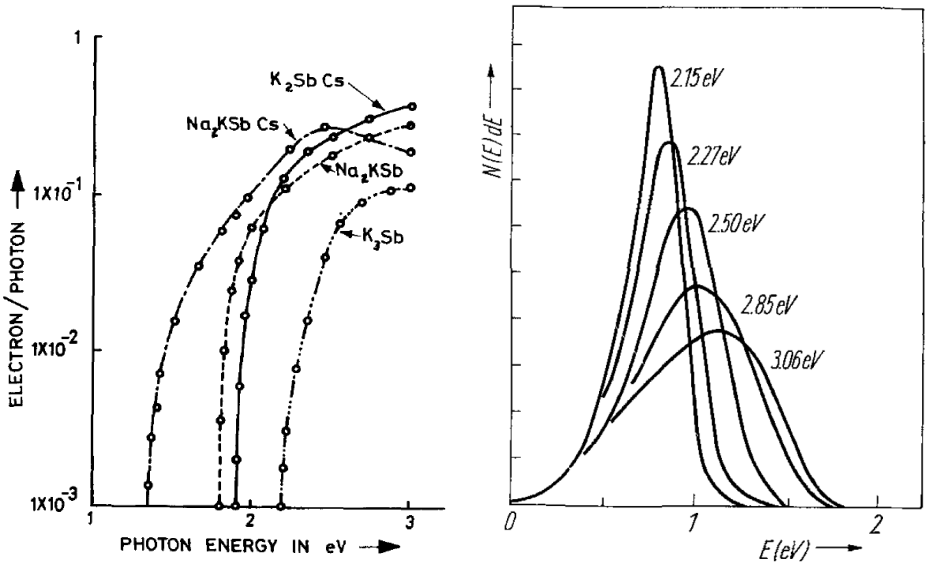

Fig. 8 The left panel shows the photoyield of a variety of alkali antimonides (from Ghosh et al. [22]). The right panel shows the photoelectron spectrum of K_2CsSb (from Nathan et al.[23])

The above figure shows electron yield curves for a number of alkali antimonides. The most sensitive at low energy is the multialkali Na_2KSbCs, but this has a relatively slow roll-off with decreasing energy, which would be expected to give a relatively wide electron kinetic energy spectrum. The bi-alkali K_2CsSb discovered by Sommer [24] has a rapid increase in yield with increasing photon energy, and a yield of > 10% at 532 nm. This wavelength is important because we have to consider the type of laser used for excitation. The most convenient to use will be a fiber laser, due to the very high reliability, small size and low cost of these systems (commercial 1 MHz, 1 μJ lasers with wavelengths from 1030 to 1064 nm are available). Including frequency doubling (25%), longitudinal (10% with a birefringent pulse stacker) and transverse shaping (using Pi-shapers for example) and optical losses, this laser – antimonide combination will produce pulse charges of several nC at MHz rates. The emittance is related directly to the product of the beam radius and the square root of the excess kinetic energy of the photoelectrons when initially emitted. We cannot reduce the beam radius at the cathode beyond a certain point due to space charge reduction of the accelerating gradient, and typically for nC pulse charge with 20 MV/m accelerating gradient, this value should be around 1 mm. This sets the required energy width to be < 1 eV for 1 μm-rad normalized emittance. From the work of Nathan shown above, aiming for the 'thermal' emittance to contribute at most 50% of the total emittance, we would need to be at < 2.5 eV (ie. > 500 nm wavelength). This value has to be corrected for the substantial (1/10s of an eV) Schottky barrier lowering caused by the accelerating field. We can see that to determine the incident wavelength, we need very precise information on the yield vs. wavelength and the photoelectron energy distribution. In order to model emittance correctly, we also need information on the full momentum distribution of the electrons, ie. we should not assume isotropic angular distributions; as we make more single crystal-like materials, we can expect band-structure effects to be seen in the angular distributions. We also need to be aware that this material can exist in several crystallographic forms and that small changes in stoichiometry may well change the properties significantly. This can be seen graphically in comparisons of the electronic structure of Cs-K-Sb compounds calculated with state of the art density functional methods [25] (full potential, linearized augmented plane wave [FP-LAPW] combined with generalized gradient method [GGG] as used in Wien2k: see http://www.wien2k.at/). This material also has the useful property that the dark current at room temperature is low compared to the multi-alkali materials, presumably due to the slightly larger band-gap and the degree of perfection with which the material can be grown. It should be noted that the majority of these studies have been performed on glass substrates due to the application to photo-multipliers and optical devices, or on ultrathin amorphous carbon substrates for electron diffraction studies[26, 27]. For photo-gun applications, we need a robust thick metallic substrate, and thus it is quite likely that the growth mode will be very different between transmission and reflection cathodes. Indeed, we see large variability in our own work depending on the particular type of metallic or semiconductor substrate used. In our work [28-31] and in the work of the Cornell ERL group [32, 33], we have demonstrated high QE

and low emittance, as well as sustained high current operation. However a huge amount remains to be done to fully understand the chemistry of this complex materials and then to optimize them for high gradient photoinjectors. For example, the standard thermal growth methodology always seems to result in a rough surface. This has been measured by in-situ AFM, and its effects on emittance growth have been measured [34]. We need to understand how to precisely control stoichiometry, how to grow very smooth films to avoid high gradient emittance growth, and ultimately to grow single crystal single domain materials to allow us to take advantage of band effects which can dramatically reduce emittance.

Progress under this grant

In the past three years, this project has made great strides in understanding the structure and chemistry of the alkali antimonides. Several techniques have been employed, across two systems, to observe cathode growth *in operando/in situ* during formation. X-ray diffraction (XRD) has been used to measure grain size and texture, crystallization threshold and time evolution of cathode chemistry during growth. X-ray reflectivity (XRR) and grazing incidence small angle x-ray scattering (GISAXS) have been used to measure the evolution of film thickness and roughness. The application of these techniques to cathode growth was developed at the National Synchrotron Light Source (NSLS), and was recently successfully demonstrated at the Cornell High Energy Synchrotron Source (CHESS), providing additional resources and capability for this program. In parallel, *in situ* x-ray photoemission spectroscopy (XPS) and atomic force microscopy (AFM) has been undertaken at the Center for Functional Nanomaterials (CFN) to characterize the chemical evolution of the cathodes, observe variations between surface and bulk stoichiometry, and measure the "local scale" roughness (as opposed to the roughness measured by XRR, which has a much longer correlation length). Extensive effort has also gone into understanding the roughness evolution of the cathodes, including investigation of the initial structure of antimony films under various deposition conditions using *ex situ* AFM and XRR. Work at LBNL has focused on production of high yield films and measurement of their emittance and the effects of high gradient fields on emittance. In addition, the LBNL work has branched out into the production of bulk alkali antimonides by solid state synthesis, and in measurement of nano-scale roughness using Grazing Incidence Small Angle X-ray Scattering during growth, and by AFM.. In the following we will illustrate a few aspects of this work.

In the course of this work, it was necessary to develop a new tool/end-station vacuum system for the NSLS/CHESS measurements (below), which has allowed us to reach vacuum levels (0.2 nTorr) suitable for alkali antimonide growth. This new apparatus allows cathode growth for and transfer to the 112 MHz SRF gun, and is fully compatible with the cathode transport system.

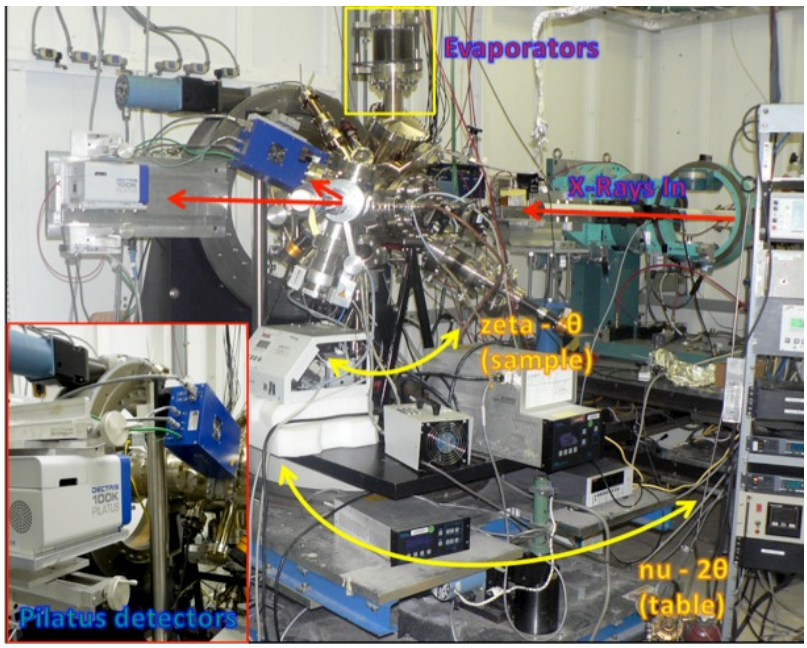

Fig. 9 The experimental set up at the X21 beamline at NSLS. A 4 axis diffractometer with a UHV chamber allows the *in-situ* x-ray diffraction characterization of cathode growth. Inset: Position of the two Pilatus cameras placed after the beryllium X-ray exit window of the chamber.

This system has been used to successfully grow ~10 alkali antimonide cathodes, with QE up to 6.3% @ 532 nm. A composite wide angle XRD pattern is shown below from both cameras after each stage of cathode growth.

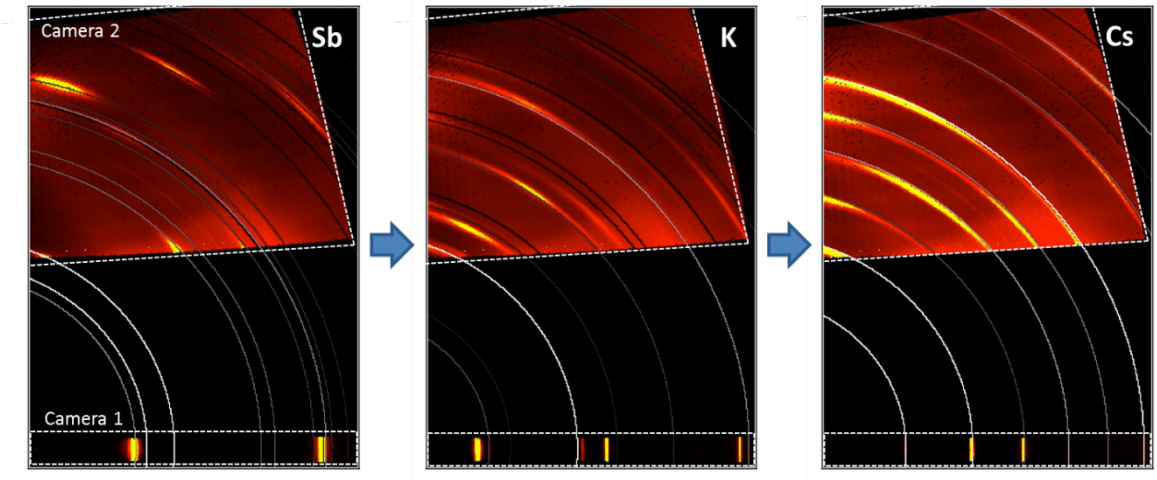

Fig. 10 XRD of an alkali antimonide cathode after each stage of growth. The initial Sb film is shown on the left, with a [003] surface texture. The white lines show the expected Sb pattern if the film were untextured. The red areas are the areas of scattering space covered by the two cameras. The center shows post K deposition, along with the expected K_3Sb pattern. The right shows the final cathode structure – with a mixed [220] and [222] texture, along with the expected rings for K_2CsSb. This cathode achieved a QE of 6.3% at 532 nm.

We can clearly show that the production of K_2CsSb under optimum conditions passes through a phase where we have produced only weakly ordered K_3Sb consisting of several phases. Reaction with Cs then drives the compound into an ordered phase. The dynamics of formation of K_2CsSb depend on a host of conditions, such as initial structure of the Si surface, the structure of the initial antimony film, rate of deposition and temperature trajectory. Our ultimate aim is to understand this complex reaction surface so that we can control and optimize the material, for example by controlled doping, and epitaxial growth.

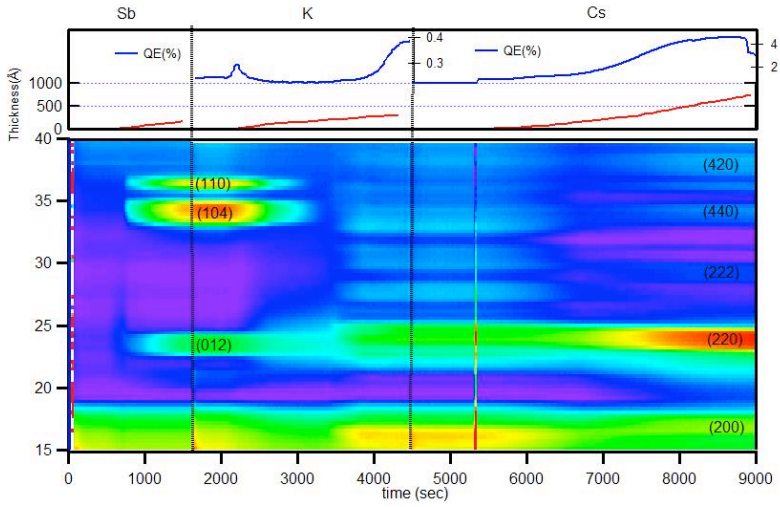

Fig 11. XRD time sequence of cathode growth, showing the onset of Sb crystallization (700s), the dissolution
of Sb caused by the addition of Potassium (3000s), the formation of K3Sb (3500s) and the conversion
to K2CsSb (7500s). The deposition rates and QE are plotted above, on the same timescale.

The complexities of the synthesis can be seen in Fig 11, which shows am XRD time sequence of one whole reaction, from crystallization of the Sb from its amorphous initial state, through reaction to give a relatively disordered K-Sb phase, to the final delayed onset reaction to form the final compound.

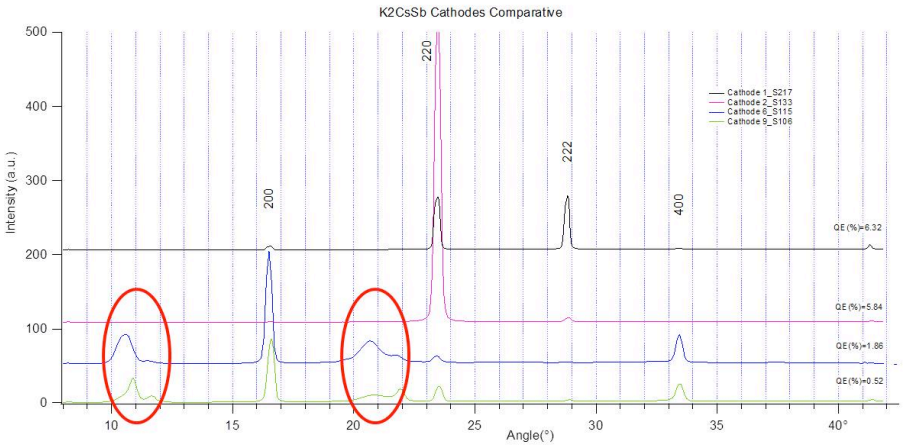

Fig. 12 XRD of four alkali antimonide cathodes after growth. The labeled peaks correspond to K_2CsSb, while those circled in red are unrelated. The QE at 532 nm is shown for each cathode.

This complexity is emphasized in Fig 12, where 4 compounds grown under slightly different conditions of initial Sb growth and temperature, form rather different final compounds, as revealed through dynamic in-situ XRD.

XRD only tells some of the story of these systems, as it reveals primarily information about atomic structure. Information on the nanostructure of the material and growth mode can be revealed through x-ray reflectively (XRR), or more generally through grazing incidence small angle x-ray scattering (GISAXS). Specular x-ray reflectivity dynamically measures the thickness of a growing film. GISAXS reveals information on the in and out of plane roughness and domain size.

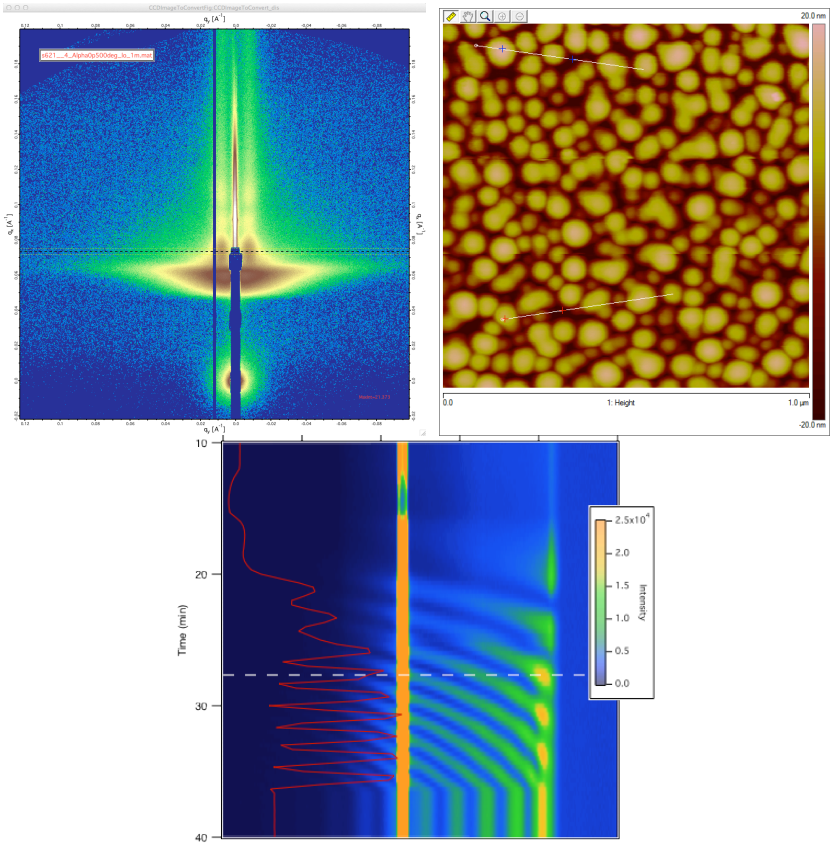

Fig. 13 Center panel is an AFM image of a nominally 10 nm thick Sb film grown a room temperature, left, we show the corresponding GISAXS I(q_y, q_z)pattern, and at the right,
a cut at $q_y = 0$ of q_z as a function of time.

For example, in Fig. 13 we show the GISAXS pattern at 0.3 degrees grazing angle, 10 keV photon energy, of a nominally 10 nm thick Sb film. Under the substrate, rate and temperature conditions used, this film breaks up immediately into island growth. The GISAXS shows a strong Yoneda peak related to roughness, a $q_y = 0$ peak and two side bands in q_y. The position of these bands gives the average lateral size of the islands that have been formed, and the oscillations in q_z give information on the island height. We are using codes developed at LBNL for very rapid real time analysis of GISAXS, so that we can have real-time feedback in thin film growth. The code we are using is based on the distorted wave Born approximation, and is implemented on a high performance computer at NERSC [35]. This information can be gathered in-situ as the film grows and is a perfect tool for monitoring and controlling roughness at all stages of growth. Minimizing roughness is a key aim in producing cathodes suitable for high gradient photoguns.

The work at the CFN has focused on *in situ* X-ray Photoemission Spectroscopy (XPS) and Atomic Force Microscopy (AFM). The AFM measurements have resulted in a

new understanding of the level of roughness inherent in alkali antimonide cathodes and is complementary to in-situ GISAXS.

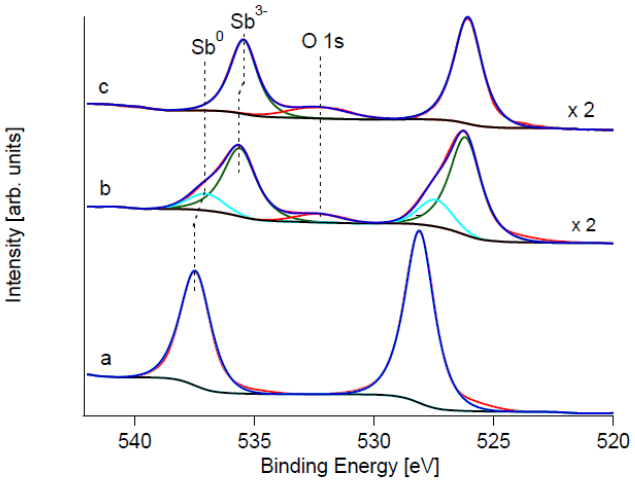

Fig. 14 XPS Sb 3d spectra; (a) after Sb deposition on Si(100), (b) after K deposition and (c) after Cs deposition. The very strong core level shift on K reaction, and the weaker
shift on Cs reaction can be seen, as well as reaction with a small amount of residual oxygen

Following the same methodology used in the X21 experiments, the growth steps were evaluated with a focus on the chemical composition of the surface layer. XPS measurements were performed after each evaporation step and the Sb 3d, K 2p, Cs 3d and Si 2p region were examined. From the ratios of the area of the fitted peaks the composition was determined. The intermediate step, after Potassium deposition, consists of $K_{2.4}Sb$ and Antimony in the metallic state, which did not react with Potassium. After Cesium deposition all of the Antimony in the surface layer is reduced. The ratio of the Alkali in the surface region is with $Cs_{2.1}K_{1.1}Sb$ reverse to the bulk stoichiometry. From the growth chamber the cathode can be transferred into an UHV-AFM without exposure to air. This has shown that as confirmed by GISAXS, the material grows in islands and does not form a uniform defect free surface.

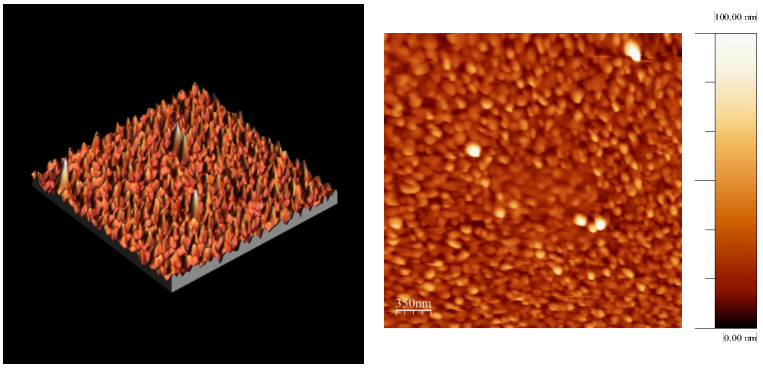

Fig 15 AFM of an alkali antimonide cathode after growth. This cathode has a nominal

thickness of 25 nm, and an RMS roughness of 11.5 nm with 100 nm spatial period.

We have transported two K_2CsSb cathodes grown at BNL to JLAB for testing in a DC injector at 200 keV [31]. These tests proved that vacuum transport can work for this material; the cathodes arrived with a QE at 532nm of >1%. This cathode achieved 20 mA average current, with a charge lifetime far in excess of similar GaAs cathodes. The figure below shows a QE map and current lifetime measurement at 5 mA from this test. The lifetime of the cathode in these tests was limited by laser heating - suggesting that a substrate of higher thermal conductivity may allow higher operational currents.

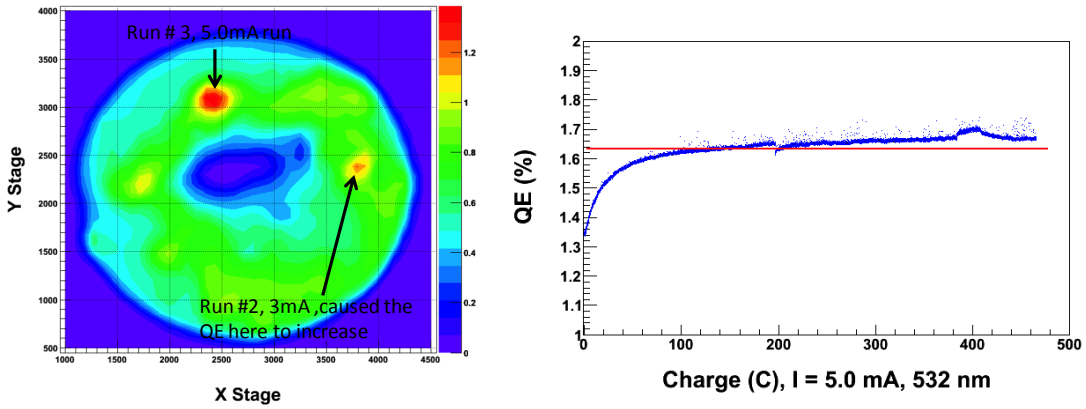

Fig 16 QE map at 532 nm, in Jlab 200 keV DC gun. The center of the cathode was damaged in a vacuum event in the gun, but the bulk of the cathode was unharmed. The charge lifetime at 5 mA
unlimited within the time that the measurement was made

As well as the structural studies and studies of lifetime, we have continued lab-based measurements of emittance. We have measured an emittance of 0.36 microns at 532 nm at zero field [29]and in order to test the 3 step model, and to test the precision of these measurements, we have extended this work to Sb metallic surfaces. Fig 17 shows a measurement of emittance as a function of photon energy for oxidized Sb, compared to a 3 step theory including the effect of kT. The data closely matches theory and reaches a minimum of around 0.25 microns, for zero excess energy. These studies validate the emttance measurement method and in the future will allow detailed measurements on the effect of variation in the materials synthesis on emittance and the distribution of transverse momentum.

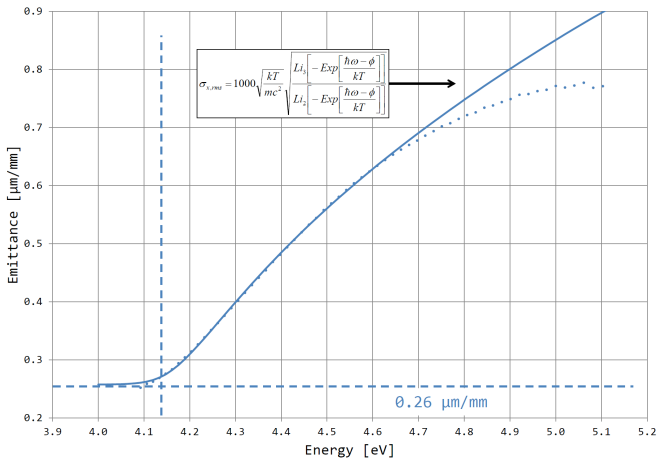

Fig. 17 Measurement of emittance in oxidized Sb as a function of photon energy

Finally we have started to make alkali antimonides by bulk synthesis method in which bulk materials in gram quantities are weighed out in an oxygen / water free glovebox, sealed in a quartz tube, and transferred to an oven. Fig. 17 (right) shows the powder pattern (superimposed on the diffuse pattern of mylar) of K_3Sb, produced by a reaction at 250C for 4 hours. The aim of this work is to be able to reliably form alkali antimonides with control over stoichiometry at the level of << 1%, We will be attempting to produce thin films using this method using thermal evaporation or pulsed laser deposition.

4.2c) Gun Transfer systems and injector testing

In order to compare the performance of multi-alkali cathodes in different gun environments and establish the cathode characteristic before and after operation in the gun, it is important to grow all of them in one growth chamber and characterize each one identically, transport them to the gun and bring them back for characterization post-use. To accomplish this we have designed and fabricated two detachable load-lock chambers, one to transport cathodes between the fabrication chamber and DC gun and another between fabrication chamber and 112 MHz SRF gun. Since the design and construction of the detachable load-lock chamber and cathode puck for 704 MHz SRF injector significantly predates that of the cathode fabrication chamber, pre- and post-characterization of the cathodes for this gun will not be accomplished at present. In the following section, the design and the operational status of each of the load-lock systems are described.

DC Gun: BNL and JLab had established a collaboration to test the multii-alkali cathodes grown at BNL to be tested at JLab in the DC test gun operating at 100 KV and 200 KV. The primary constraints in designing the load-lock system for this gun were the transfer mechanism should be compatible with the existing system and the cathode puck should be able to the hold-off the high voltages encountered in the DC gun. These were addressed by using the same transfer suitcase that was used in CEBAF and the puck design was similar to the pucks used at JLab with GaAs, but

were made of aluminum with a thin layer of stainless sheet explosion bonded to the surface to act as the substrate for the K_2CsSb cathode. The transfer suitcase consists of a manipulator, vacuum plenum and an all-metal gate valve (schematic shown in Figure below). The vacuum plenum with 20L/s ion pump and a 600 L/s NEG pump provided a base pressure of 10^{-11} Torr in the suitcase.

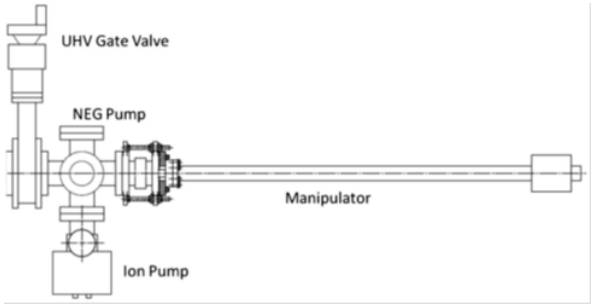

Fig. 18. Schematic of gun vacuum suitcase

With this assembly, we were able to transport two cathodes fabricated at BNL to JLab and demonstrate that the cathode performance is not affected during transfer and the cathode was robust enough to sustain even after a few vacuum spikes (see results above). The cathode was able to deliver up to 10 mA without any measurable change in the QE, corresponding to an average DC current of 8 A/cm^2.

112 MHz gun: 112 MHz SRF gun was built to provide the electron beam to increase the luminosity of the Relativistic Heavy Ion Beam (RHIC) at BNL by coherent electron cooling. The photocathode needs to be inserted into this quarter wave resonator cavity. The constraints for the cathode insertion are a) particulate free insertion to preserve the Q of the SRF cavity, b) ability to operate in field gradients > 20 MV/m and c) thermally isolated from the cavity wall. Figure 19 shows a drawing of the insertion device. The load-lock chamber containing the cathode, the magazine and cathode puck are shown in Figure 20. The magazine that can store up to 5 cathodes reducing the down time, once the load-lock is in place. The puck design is very similar to that of the DC gun and both the pucks can be inserted into the fabrication chamber for evaporating and characterizing the cathode

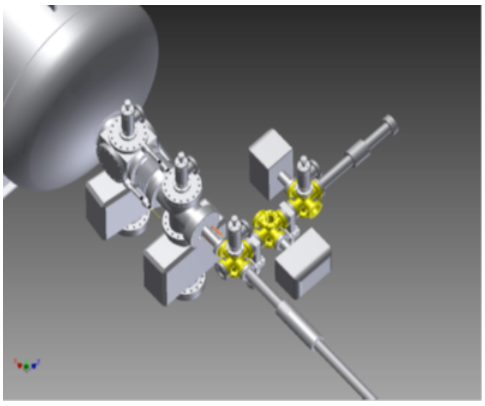

Fig 19. Design of the detachable load-lock

Fig. 20. Photograph of the load-lock

system for 112 MHz SRF gun. The manipulator in the bottom right quadrant transfers the cathode from the load-lock chamber at the top right quadrant to the gun in the top left quadrant

chamber with the magazine in the foreground. Two Mo pucks and two pucks for diamond are mounted on the magazine. This system can also mount diamond pucks described below.

704 MHz injector: The SRF gun for the 704 MHz injector is a half-cell elliptical cavity, designed to deliver up to 0.5 A current, in which the photocathode inserted as a part of a quarter wave choke joint. A photograph of the transport section and a drawing of the cathode connection are shown in Figures 21 and 22.

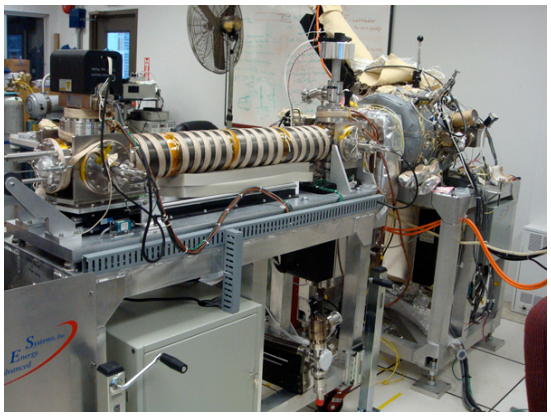

Fig 21. Photograph of the transport cart (in the foreground) and deposition chamber (back)

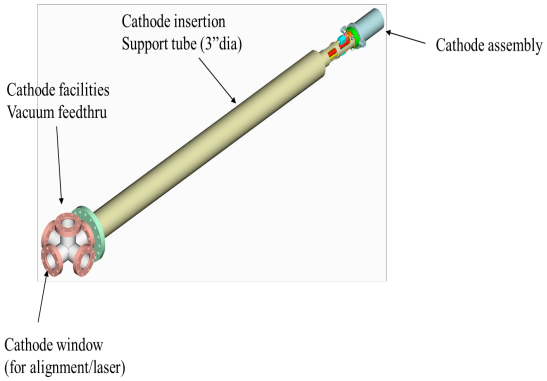

Fig. 22. Drawing of the cathode connector

Multiple K_2CsSb photocathodes have been grown with this deposition chamber. The transport cart has been tested for UHV operation. Insertion of a cathode is scheduled for the near future.

Laser systems: Two laser systems, one for the 112 MHz gun and another for 704 MHz injector are available for the electron emission. Both the lasers deliver optical beam at 532 nm and their repetition rate can be synchronized to either the gun frequency or its sub harmonic. The optical transport for the 704 MHz system is in place and that for 112 MHz gun has been designed and will be in place shortly.

Diamond amplifier capsule design and test

Diamond amplifier capsules are designed for test diamond amplifier in SRF gun. The capsule including diamond holder, mirrors to reflect laser and metal photocathode to generate primary electron current. The copper cathode is biased at -5kV and diamond holder is grounded. The primary electrons are accelerated by the electric field, and focused onto the diamond via a Peirce geometry cathode. The secondary electrons are emitted out from diamond emission surface into the gun. The mirror and cathode angle have been tested for laser and primary beam. We used UV light to test the primary electrons generation and demonstrated that the laser beam can reflect from the capsule and the electron beam arrive the diamond at the centre.

These amplifiers can be loaded into the 112 MHz gun described above with the same garage apparatus shown

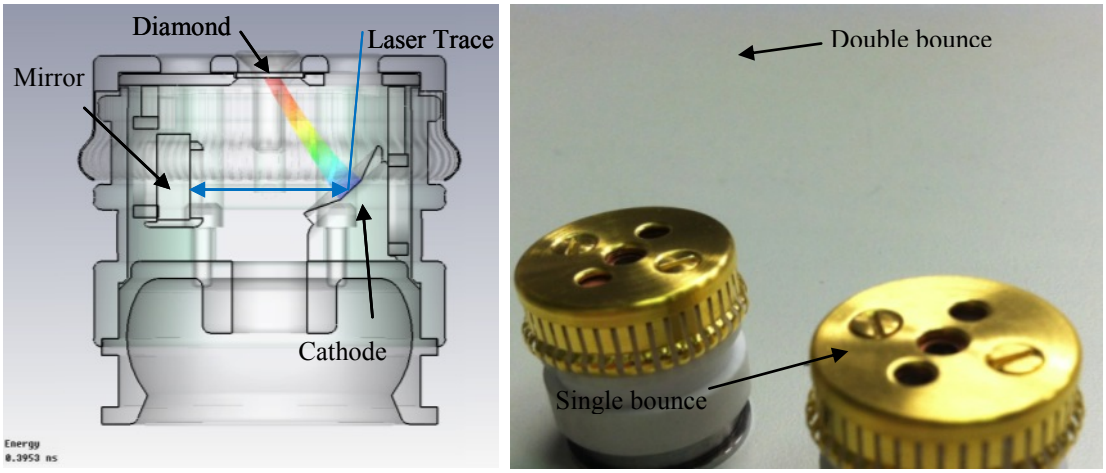

Fig 23. Left: The beam dynamics simulation on the primary beam in the capsule. The rainbow is the electron trajectory. Right: The fabricated diamond amplifier capsules

Diamond amplifier preparation

For RF gun application, the diamond thickness is limited by the transit time of the secondary electrons through the diamond. The electron drift is saturated at 2.7×10^5m/s and is independent of temperature when the external field is above 2MV/m. To meet the requirement of electric field magnitude inside the diamond and optimized initial phase for 112MHz gun, the maximum diamond thickness is 120μm. To obtain the maximum gain for relatively low energy primaries (5 keV), photolithography was employed to produce a mesh Pt coating. The meshed Pt coating will generate a relatively smooth internal field in the diamond, while reducing the primary electron energy deposited in the metal. The fig. below shows the Pt coating pattern. The thickness of the metal mesh is 30nm.

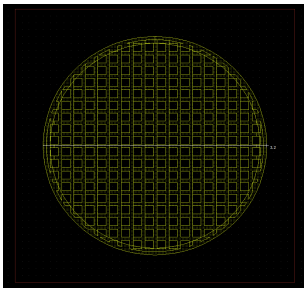

Fig. 24. Photolithography pattern. The mesh street size is 50μm, the open side is120μm. 50% diamond area was covered by the Pt.

At LBNL, the VHF 187 MHz gun has been completed and is operational and has been equipped with a cathode transport and load-lock system (designed at INFN and similar to FLASH system). It has been successfully tested with Mo and cesium

telluride cathodes, and we are now moving on to first tests on alkali antimonides. To allow this to happen, a gun deposition system was constructed with a similar transport and load lock system to the gun. This is shown in Fig. 25. The system is operational, and we expect to be transporting cathodes to the VHF gun shortly. We have also developed a new cathode plug, based on diamond turned Aluminum, that is then Molybdenum ion plated to form an unreactive surface. This circumvents problems due to the relatively poor polished surface that is achievable on native Mo.

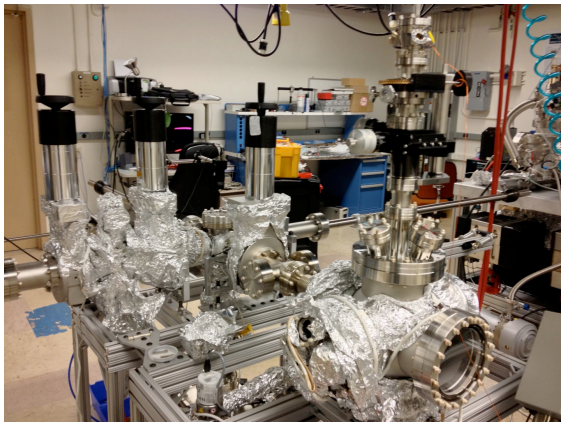

Fig. 25 This shows the gun deposition system that is used in conjunction with a similar transport system on the LBNL VHF gun.

4.3 References

1. *Next-Generation Photon Sources for Grand Challenges in Science and Energy, Report of the Workshop on Solving Science and Energy Grand Challenges with Next-Generation Photon Sources*. in*, Report of the Workshop on Solving Science and Energy Grand Challenges with Next-Generation Photon Sources*. 2008 Rockville, Maryland
2. *Committee on a Scientific Assessment of Free-Electron Laser Technology for Naval Applications, National Research Council* *http://www.nap.edu/catalog.php?record_id=12484*.
3. Akre, R., et al., *Commissioning the Linac Coherent Light Source injector.* Physical Review Special Topics - Accelerators and Beams, 2008. **11**(3): p. 030703.
4. Hernandez Garcia, C., *Status of the Jefferson Lab ERL FEL DC photoemission guns*, in *2009 ERL workshop, Ithaca, NY*2009.
5. Ivanisenko, Y., *Recent gun characterization results at PITZ*, in *FLS Workshop*2010: SLAC.
6. Dowell, D.H., S.Z. Bethel, and K.D. Friddell, *Results from the average power laser experiment photocathode injector test.* Nucl. Inst. Meth., 1995. **356**(2-3): p. 167-176.
7. Smedley, J., et al., *Diamond Amplified Photocathodes.* Mater. Res. Soc. Symp. Proc, 2009. **1039**: p. 1039-P9-02.

8. Yater, J.E., et al., *Effect of material properties on low-energy electron transmission in thin chemical-vapor deposited diamond films.* Journal of Applied Physics, 2005. **97**(9): p. 093717-9.
9. Muller, E.M., et al., *Electronic Impact of Inclusions in Diamond.* MRS Online Proceedings Library, 2009. **1203**: p. null-null.
10. Dimitrov, D.A., et al., *Simulations of Charge Gain and Collection Efficiency from Diamond Amplifiers.* MRS Online Proceedings Library, 2009. **1203**: p. null-null.
11. Muller, E.M., et al., *Transmission-mode diamond white-beam position monitor at NSLS.* Journal of Synchrotron Radiation, 2012. **19**(3): p. 381-387.
12. Bohon, J., E.M. Muller, and J. Smedley, *Development of diamond-based X-ray detection for high-flux beamline diagnostics.* Journal of Synchrotron Radiation, 2010. **17**(6): p. 711-718.
13. Keister, J.W. and J. Smedley, *Single crystal diamond photodiode for soft X-ray radiometry.* Nucl. Instrum. Meth. , 2009. **606**(3): p. 774-779.
14. Chang, X., et al. *Recent progress on the diamond amplified photo-cathode experiment*. in *Particle Accelerator Conference, 2007. PAC. IEEE*. 2007 p. 2044-2046
15. Chang, X., *Electron beam emission from a Diamond-Amplifier Cathode.* Physical Review Letters, 2013. **under review**.
16. Rameau, J.D., et al., *Properties of Hydrogen Terminated Diamond as a Photocathode.* Physical Review Letters, 2011. **106**(13): p. 137602.
17. Rumaiz, A.K., et al., *Band alignment of atomic layer deposited HfO[sub 2] on clean and N passivated germanium surfaces.* Applied Physics Letters, 2010. **97**(24): p. 242108.
18. Wang, E.G., et al., *Secondary-electron emission from hydrogen-terminated diamond: Experiments and model.* Phys.Rev, ST - Accel. and Beams, 2011. **14**(11): p. 111301.
19. Wang, E.G., et al., *Systematic study of hydrogenation in a diamond amplifier.* Phys. Rev. ST Accel. Beams, 2011. **14**(6): p. 061302.
20. Gorlich, P., Z. Phys., 1936. **101**: p. 335.
21. Sommer, A.H., *Photoemissive Materials*1968, New York: John Wiley.
22. Ghosh, C. and B.P. Varma, *Preparation and study of properties of a few alkali antimonide photocathodes.* Journal of Applied Physics, 1978. **49**(8): p. 4549.
23. Nathan, R. and C.H.B. Mee, *The energy distribution of photoelectrons from the K2CsSb photocathode.* physica status solidi (a), 1970. **2**(1): p. 67-72.
24. Sommer, A.H., *A new alkali antimonide photoemitter with high sensitivity to visible light.* Applied Physics Letters, 1963. **3**(4): p. 62-63.
25. Kalarasse, L., B. Bennecer, and F. Kalarasse, *Optical properties of the alkali antimonide semiconductors Cs3Sb, Cs2KSb, CsK2Sb and K3Sb.* Journal of Physics and Chemistry of Solids, 2010. **71**(3): p. 314-322.
26. Beck, A.H. and J.C. Robbie, *A scanning electron diffraction system for in-situ alkali antimonide photocathode studies.* International Journal of Electronics, 1972. **33**(4): p. 361-370.

27. Robbie, J.C. and A.H. Beck, *Scanning electron diffracyion studied on ceasium antimonide photocathodes during formation.* J. Phys. D: Appl. Phys., 1973. **6**: p. 1381-1392.
28. Liang, X., et al., *Deposition and In-Situ Characterization of Alkali Antimonide Photocathodes.* IPAC 2012, 2012.
29. Vecchione, T., et al., *A low emittance and high efficiency visible light photocathode for high brightness accelerator-based X-ray light sources.* Applied Physics Letters, 2011. **99**: p. 034103.
30. Smedley, J., et al., *High efficiency visible photocathode development.* PAC 2011, 2011.
31. Mammei, R.R., et al., *Charge lifetime measurements at high average current using a K_{2}CsSb photocathode inside a dc high voltage photogun.* Physical Review Special Topics - Accelerators and Beams, 2013. **16**(3): p. 033401.
32. Bazarov, I., et al., *Thermal emittance measurements of a cesium potassium antimonide photocathode.* Applied Physics Letters, 2011. **98**(22): p. 224101-3.
33. Cultrera, L., et al., *Photocathode behavior during high current running in the Cornell energy recovery linac photoinjector.* Physical Review Special Topics - Accelerators and Beams, 2011. **14**(12): p. 120101.
34. Vecchione, T., et al., *Effect of roughness on emittance of potassium cesium antimonide photocathodes.* IPAC 2012, New Orleans, 2012.
35. Chourou, S. T., et al., *HipGISAXS: A High-Performance Software for Simulating GISAXS Data.* Journal of Computational Physics, 2013.
36. McCarroll, W.H., *Chemical and structural characteristics of the potassium-cesium-antimony photocathode.* Journal of Physics and Chemistry of Solids, 1965. **26**(1): p. 191-195.
37. di Bona, A., et al., *Development, operation and analysis of bialkali antimonide photocathodes for high-brightness photo-injectors.* Nucl. Instrum. Methods, 1997. **A385**(3): p. 385-390.
38. Lyashenko, A., et al., *Ion-induced secondary electron emission from K--Cs--Sb, Na--K--Sb, and Cs--Sb photocathodes and its relevance to the operation of gaseous avalanche photomultipliers.* Journal of Applied Physics, 2009. **106**(4): p. 044902.
39. Sommer, A.H., *Characteristics of Evaporated Antimony Films as a Function of the Antimony Source.* Journal of Applied Physics, 1966. **37**(7): p. 2789-2791.
40. Sommer, A.H. and W.H. McCarroll, *A New Modification of the Semiconducting Compound K[sub 3]Sb.* Journal of Applied Physics, 1966. **37**(1): p. 174-179.
41. Night, C., *A field where jobs go begging,* Symmetry Magazine http://www.symmetrymagazine.org/cms/, 2010.

5. Products.

1. D. Kayran et al., SRF Photoinjector for Proof-of-principle Experiment of Coherent Electron Cooling at RHIC, IPAC2012, New Orleans (2012).
2. T. Vecchione et al., Effect of Roughness on Emittance of Potassium Cesium Antimonide Photocathodes, IPAC2012, New Orleans (2012).

3. X. Liang et al., Deposition and In-Situ Characterization of Alkali Antimonide Photocathodes, IPAC2012, New Orleans (2012).
4. T. Vecchione et al., A low emittance and high efficiency visible light photocathode for high brightness accelerator-based X-ray light sources, *Appl. Phys. Lett.* **99**, 034103 (2011).
5. H.A. Padmore et al., High QE, Low Emittance, Green Sensitive FEL Photocathodes Using K_2CsSb, FEL2011, Shanghai, China (2011).
6. R. Mammei et al., Charge Lifetime Study of K2CsSb Photocathode Inside a JLAB DC High Voltage Gun, Proceedings of IPAC2011, San Sebastián, Spain (2011).
7. J. Smedley et al., High Efficiency Visible Photocathode Development, Proceedings of IPAC2011, San Sebastián, Spain (2011).
8. M. Gaowei et al., Annealing dependence of diamond-metal Schottky barrier heights probed by hard x-ray photoelectron spectroscopy, *Appl. Phys. Lett.* **100**, 201606 (2012).
9. R. R. Mammei et al., Charge lifetime measurements at high average current using a K2CsSb photocathode inside a dc high voltage photogun, *Phys. Rev. ST Accel. Beams* **16**, 033401 (2013).
10. W. Xu et al., Multipacting simulation and test results of BNL 704 MHz SRF gun, IPAC2012, New Orleans (2012).
11. E. Wang et al., Secondary-electron emission from hydrogen-terminated diamond, IPAC2012, New Orleans (2012).
12. T. Xin et al., Simulations of multipacting in the cathode stalk and FPC of 112 MHz superconducting electron gun, IPAC2012, New Orleans (2012).
13. D. A. Dimitrov et al, Modeling if Diamond Based Devices for Beam Diagnostics, Proceedings of 2011 Particle Accelerator Conference, New York, NY, USA (2011).
14. D. A. Dimitrov et al., Simulations of Surface Effects and Electron Emission from Diamond-amplifier Cathodes, Proceedings of IPAC2011, San Sebastián, Spain (2011).
15. T. Vecchione et al., High QE, Low Emittance, Green Sensitive FEL Photocathodes using K_2CsSb, Proceedings of FEL2011, Shanghai, China (2011).
16. E. Wang et al., Systematic study of hydrogenation in a diamond amplifier, Phys. Rev. ST Accel. Beams **14**, 061302 (2011).
17. E. Wang et al., Secondary-electron emission from hydrogen terminated diamond: Experiments and model, Phys. Rev. ST Accel. Beams **14**, 111301 (2011).
18. S. Belomestnykh et al., Superconducting 112 MHz QWR electron gun, 15th International Conference on RF Superconductivity (SRF2011), Chicago, Illinois (2011).
19. T. Xin et al., Design of the fundamental power coupler and photocathode inserts for the 112MHz superconducting electron gun, 15th International Conference on RF Superconductivity (SRF2011), Chicago, Illinois (2011).
20. E. Wang et al., Progress on diamond amplified photo-cathode, Proceedings of 2011 Particle Accelerator Conference, New York, NY, USA (2011).

6. Acronyms

AFM	Atomic force microscope
ALS	Advanced Light Source (LBNL)
ARPES/UPS	Angle resolved photoemission spectroscopy/ Ultraviolet Photoemission Spectroscopy
BCP	Buffered chemical polishing
BNL	Brookhaven National Laboratory
CASE	Center for Accelerator Science and Education (at Stony Brook)

CCD	Charge coupled device
CVD	Chemical vapor deposition
DC/CW	Direct current/continuous wave, often referring to continuous
DFT	Density functional theory
EBIC	Electron beam induced current
ERL	Energy recovery linac (linear accelerator)
EXAFS	Extended X-ray absorption fine structure
FEL	Free electron laser
GISAXS	Grazing incidence small angle X-ray scattering
Jlab	Thomas Jefferson National Accelerator Facility
LBNL	Lawrence Berkley National Laboratory
LCLS	Linac Coherent Light Source (SLAC)
LEED	Low energy electron diffraction
NEG	Non-evaporable getter (vacuum pump)
NEXAFS	Near edge X-ray absorption fine structure
NSLS	National Synchrotron Light Source (BNL)
PEA/NEA	Positive electron affinity/negative electron affinity
PEEM	Photoemission electron microscope
PLD	Pulsed laser deposition
RBS	Rutherford backscattering spectrometry
SBU	Stony Brook University
SEM/TEM	Scanning electron microscope/transmission electron microscopy
SIMS	Secondary ion mass spectroscopy
SLAC	Stanford Linear Accelerator Center
SRF	Superconducting radio frequency
STM	Scanning tunneling microscope
UHV	Ultra-high vacuum (typically nTorr or better)
UV	Ultra-violet
VHF	Very high frequency (normal conducting RF in this context)
XANES	X-ray absorption near-edge spectroscopy
XAS	X-ray absorption spectroscopy (includes EXAFS and XANES/NEXAFS)
XPS	X-ray photoemission spectroscopy
XRD	X-ray diffraction
XRF	X-ray fluorescence